Pergamon

Int. J. Heat Mass Transfer. Vol. 39, No. 2, pp. 259–274, 1996

0017-9310/96 $9.50+0.00

0017-9310(95)00128-X

Steady solution selection and existence in geothermal heat pipes—I. The convective case

M. J. McGUINNESS

Mathematics Department, Victoria University of Wellington, P.O. Box 600, Wellington, New Zealand

(*Received* 21 *April* 1994 *and in final form* 15 *March* 1995)

Abstract—Steady heat pipe solutions with capillarity and conduction effects included are considered. A single layer model is studied as a singular perturbation problem, with capillary boundary layers in the temperature-saturation phase plane leading to new insights and results. In the geothermal context, with bottom heating and heat flow that is dominated by convection, phase plane trajectories of temperature vs saturation typically track zero capillarity (gravity-driven) solutions when they exist, one liquid-dominated and one vapor-dominated. The way in which choice of boundary conditions selects from these solutions is studied. Capillary boundary layers, not encountered in previous studies, play an important role in this selection process. Maximum possible lengths of heat pipes are calculated, in cases where it has previously been speculated that the lengths may be unbounded.

1. INTRODUCTION

In a heat pipe, it is possible to transfer heat with very little net mass flow, by having steam and liquid flowing in opposite directions through a porous medium in contact with each other. In modeling a geothermal reservoir, the different densities of the liquid and vapor phases lead to a gravity-driven heat pipe, with liquid flowing down and vapor travelling up. Heat flow is vertically upwards, due to the specific enthalpy of steam being larger than that of liquid water. Although the system is open in general, it is typical that net mass flux is small. Such a model has been put forward by White *et al.* [1] for a part of the Geysers steam field, and also applies to Larderello in Italy, Matsukawa in Japan and Kawah Kamojang in Indonesia.

In engineering applications, the heat pipe is often driven by capillary pressure differences, due to saturation gradients, so that heat may flow horizontally or vertically downwards. The flow system is usually closed, with zero net mass flux. Applications include cold weather gloves for humans, space systems and very high speed computer chips [2–5].

In a number of studies of the heat pipe mechanism, it has become clear that in the gravity-driven case there are sometimes two solutions possible for a given steady heat flow, one vapor-dominated and one liquid-dominated. However, often only one of these solutions is actually obtained, in an experiment or in a computer study. Computer studies have involved solving both the steady-state problem, and the full time-dependent problem, which is run for long enough to achieve steady-state.

A fundamental question that arises is whether both solutions are realistic. Recent work by Satik *et al.* [6] suggests that only the vapor-dominated solution is typically obtained. Also, Schubert and Straus [7] obtain only the vapor-dominated solution when two-phase counterflowing fluid overlies stationary liquid. However, in laboratory experiments, Udell [8], Bau and Torrance [4] and Cornwell *et al.* [5] obtain only liquid-dominated solutions.

Further, Sheu *et al.* [9] find when numerically integrating the steady-state conditions down from the surface, no counterflow solutions exist when net mass flow is small. Theirs is a three-layer model, liquid–two-phase–liquid, with no capillarity. This result is apparently directly contradictory to the above results of Schubert and Straus [7]. Satik *et al.* [6] obtain vapor-dominated solutions for zero net mass flow, when integrating upwards from a liquid layer.

Two-phase solutions will be examined in a temperature-saturation phase plane, and the mechanism determining which solution is selected will become clear. The role played by capillary boundary layers is crucial, leading to a resolution of the above apparent discrepancies.

This work extends recent studies in McGuinness *et al.* [10] and McGuinness [11–13]. Capillarity was not included in those papers, but results are consistent, suggesting that the mechanism of upstream differencing studied in those papers is equivalent to introducing a numerical diffusive boundary layer, which acts to select solutions in the same way as capillarity.

The approach in this paper has been strongly influenced by the recent papers of Satik *et al.* [6] and Stubos *et al.* [14]. Their treatment is here extended and modified:

NOMENCLATURE

d	unit of permeability [1 darcy = 10^{-12} m^2]
h	specific enthalpy
h_{vl}	latent heat of vaporization
g	gravitational acceleration
J	the Leverett J-function, $1.417(1-s)-2.12(1-s)^2+1.263(1-s)^3$
k	permeability
k_r	relative permeability
md	millidarcy [10^{-3} darcy]
m_l	molecular weight of liquid water [kg kmol^{-1}]
u	mass flux density [kg s^{-1} m^{-2}]
P	pressure
P_c	capillary pressure
Q	energy flux [W m^{-2}]
R	universal gas constant [m^3 Pa K^{-1} mol^{-1}]
S	liquid saturation
T	temperature [°C]
z	vertical distance [m].

Greek symbols

β	v_l/v_v
γ	$dT/dP(v_v)/(h_{vl}\Delta\rho)$
λ	thermal conductivity
λ_l	liquid mobility, kk_{rl}/v_l
λ_v	vapor mobility, kk_{rv}/v_v
μ	dynamic viscosity
v	kinematic viscosity
ω	dimensionless heat flow $(Qv_v/(kgh_{vl}\Delta\rho)$
ϕ	porosity
ρ	specific density
σ	surface tension [kg s^{-2}].

Subscripts

l	liquid water
v	steam or vapor phase.

(1) by allowing full temperature dependence of fluid properties;

(2) by showing that the results are qualitatively independent of the forms used for the relative permeabilities and

(3) by allowing a wider range of possible heat flow rates, a consequence of using a single-layer model.

The three-layer model used in [6] limits the possible range of heat flow values through the heat pipe, and also implicitly limits solutions to those with a smooth transition from pure vapor to pure liquid. Other possibilities for what happens at the ends of the two-phase region, such as the presence of a convective higher-dimensional liquid flow, as seen in [15], or the presence of pure liquid phase in place of the vapor phase, motivate the consideration here of the two-phase region in isolation, as a single-layer model.

Satik *et al.* [6] consider two main cases, the *heat pipe case* (driven by capillary pressure) and the *geothermal case* (driven by gravity). The results in the present paper affect most significantly the geothermal case. The heat pipe case is already well understood (e.g. [21]). Note that in [6] the definitions of the *heat pipe* and *geothermal* cases involve the choice of boundary conditions when integrating the differential equations governing steady-state flow. This is different to the definitions used here, but the results presented here have suggested that definitions involving the physical driving mechanism are preferable.

Questions have also been raised in previous studies [6, 15, 8] about the maximum possible length of a heat pipe, in the geothermal case with heating from below. Sondergeld and Turcotte [15] find no upper bound to the possible heat pipe length. Udell [8] has a theoretical prediction of infinite length at dry-out, for bottom heating. In the present paper, a phase plane analysis makes it possible to calculate maximum heat pipe lengths for heat flow values through the critical dry-out value. Practical limitations on temperature range, like the disappearance of the distinction between vapor and liquid phases above critical temperature, lead to finite maximum possible lengths for heat flows below dryout values.

The analysis in this paper is confined to permeabilities greater than 1 md, which corresponds to heat flow dominated by convection. The effects of reducing permeability to values where conduction becomes more important are studied in a later paper [16].

Steady-state equations are presented in Section 2 as a pair of coupled first-order differential equations. A rescaling that emphasizes the importance of a small parameter depending on capillary pressure follows in Section 3. Section 4 contains a singular perturbation analysis of steady solutions. The implications of this for selection between vapor-dominated and liquid-dominated solutions are considered in Section 5. In Section 6, previous experimental, numerical and analytical results are clarified in light of the present study. The generality of the qualitative results obtained here under a variety of choices of relative permeability functions is discussed in Section 7. In Sections 8 and 9 there follows a discussion of how computer visualizations have helped this work, and calculations of maximum possible heat pipe lengths. A discussion of when capillary pressure and gravity assist or oppose each other in driving the counterflow is the subject of Section 10. Conclusions are presented in Section 11.

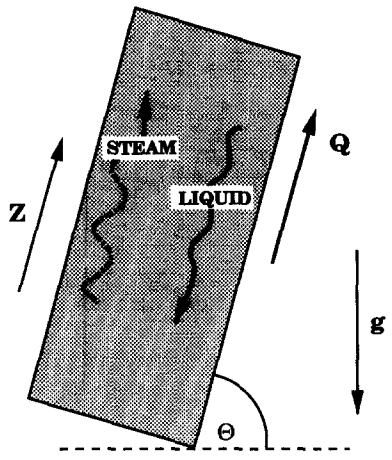

Fig. 1. A sketch illustrating the flow geometry used in the mathematical model.

2. STEADY-STATE EQUATIONS

A steady heat flux is imposed on a two-phase region, with zero net mass flux. Capillary pressure and/or gravity can drive this counterflow, so that this formulation encompasses both engineering and geothermal heat pipes.

The flow is one-dimensional, and inclined at an angle θ to the horizontal, as illustrated in Fig. 1. Steam and heat flow in the positive z direction.

Darcy's law gives the momentum balance for the two phases,

$$u_l = -\frac{kk_{rl}}{\nu_l}\left(\frac{\partial P_l}{\partial z} + \rho_l g \sin\theta\right) \tag{1}$$

$$u_v = -\frac{kk_{rv}}{\nu_v}\left(\frac{\partial P_v}{\partial z} + \rho_v g \sin\theta\right). \tag{2}$$

Capillary pressure is taken to be

$$P_c(S,T) = P_v - P_l \tag{3}$$

and the particular form for P_c is kept general at this point. Vapor-pressure lowering (the Kelvin effect) is also represented in a general way as (after ref. [17])

$$P_v = f_{vpl}(T,S)P_{sat}(T) \tag{4}$$

where the vapor-pressure lowering factor is approximated by

$$f_{vpl} = \exp\left\{\frac{-m_l P_c(S,T)}{\rho_l R(T+273.15)}\right\} \tag{5}$$

and where P_{sat} is the saturated vapor pressure of bulk liquid, obeying the Clausius–Clapeyron relation

$$\frac{dP_{sat}}{dT} = \frac{\rho_l \rho_v h_{vl}}{(T+273.15)(\rho_l - \rho_v)}. \tag{6}$$

Mass and energy conservation yield

$$u_l + u_v = 0 \tag{7}$$

$$u_v h_v + u_l h_l = Q + \lambda \frac{\partial T}{\partial z}. \tag{8}$$

See also refs. [7, 18, 19] for these. P_v and S are chosen here as the dependent thermodynamic variables. Noting that equation (4) implicitly relates T to P_v and S, and that P_c depends on P_v via T and on S [equation (3) is taken to define P_l, with P_c a known function of S, T], the dependencies of variables may be summarised as in Table 1. These dependencies determine the partial derivatives so that, for example,

$$\frac{dP_c}{dz} = \frac{\partial P_c}{\partial T}\left(\frac{\partial T}{\partial P_v}\frac{\partial P_v}{\partial z} + \frac{\partial T}{\partial S}\frac{\partial S}{\partial z}\right) + \frac{\partial P_c}{\partial S}\frac{\partial S}{\partial z}.$$

Using these dependencies, the conservation equations (7) and (8) may be rearranged to obtain

$$\frac{\partial P_v}{\partial z} = -\frac{\mathscr{H}(P_v,S)}{\mathscr{F}(P_v,S)} \tag{9}$$

$$\frac{\partial S}{\partial z} = \frac{\mathscr{G}(P_v,S)}{\mathscr{F}(P_v,S)} \tag{10}$$

where

$$\mathscr{F} = F_1 F_4 - F_3 F_2 \tag{11}$$

Table 1. Dependencies of variables.

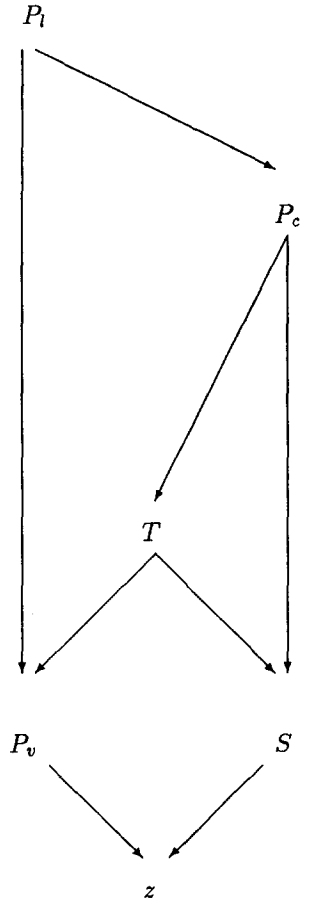

$$\mathscr{G} = G_1 G_4 - G_3 G_2 \tag{12}$$

$$\mathscr{H} = H_1 H_4 - H_3 H_2 \tag{13}$$

and

$$F_1 = \lambda_l + \lambda_v - \lambda_l \frac{\partial P_c}{\partial T}\frac{\partial T}{\partial P_v} \tag{14}$$

$$F_2 = \lambda_l\left(\frac{\partial P_c}{\partial S} + \frac{\partial P_c}{\partial T}\frac{\partial T}{\partial S}\right) \tag{15}$$

$$F_3 = \lambda_l h_l + \lambda_v h_v - \lambda_l h_l \frac{\partial P_c}{\partial T}\frac{\partial T}{\partial P_v} + \lambda \frac{\partial T}{\partial P_v} \tag{16}$$

$$F_4 = \lambda_l h_l\left(\frac{\partial P_c}{\partial S} + \frac{\partial P_c}{\partial T}\frac{\partial T}{\partial S}\right) - \lambda \frac{\partial T}{\partial S} \tag{17}$$

$$G_1 = F_1 \tag{18}$$

$$G_2 = g \sin\theta(\lambda_l \rho_l + \lambda_v \rho_v) \tag{19}$$

$$G_3 = F_3 \tag{20}$$

$$G_4 = Q + g \sin\theta(\lambda_l \rho_l h_l + \lambda_v \rho_v h_v) \tag{21}$$

$$H_1 = G_2 \tag{22}$$

$$H_2 = F_2 \tag{23}$$

$$H_3 = G_4 \tag{24}$$

$$H_4 = F_4. \tag{25}$$

Hence steady-state solutions may usefully be plotted in the P_v, S (or T, S) phase plane, as the above are two coupled autonomous nonlinear first-order differential equations. Satik *et al.* [6] study these equations with particular forms for capillary pressure (Leverett J-function), relative permeability (percolation) and the Clausius–Clapeyron equation (vapor phase as ideal gas).

Some physical meaning for the right-hand sides of these two coupled differential equations (9) and (10) can be brought out. The grouping $\mathscr{H}/(\mathscr{F} g \sin\theta)$ is an averaged flowing two-phase density, which controls the pressure gradient. The combination $\mathscr{G}/\mathscr{F}$ represents the imbalance between gravity and capillary pressure. It determines how saturation must change, in order that capillary pressure effects and gravity effects add up to give the correct heat flow through the heat pipe.

3. CAPILLARY BOUNDARY LAYERS

The right-hand sides of equations (9) and (10) have a complicated dependence on P_v and S. This dependence is simplified a little if the factor $\partial P_c/\partial S$ is extracted from the right-hand sides, and pressure is non-dimensionalized by a maximum pressure P_0 (say the critical pressure, 22.12 MPa) so that the pressure P_v^* is of order one. Then equations (9) and (10) become

$$\frac{\partial P_v^*}{\partial z^*} = -\frac{\mathscr{H}^*(P_v^*, S)}{\mathscr{F}^*(P_v^*, S)} \tag{26}$$

$$\varepsilon \frac{\partial S}{\partial z^*} = \frac{\mathscr{G}^*(P_v^*, S)}{\mathscr{F}^*(P_v^*, S)} \tag{27}$$

where

$$\mathscr{F}^* = \frac{P_0}{H_0}\left[\lambda_l\left(1 - \frac{\partial P_c}{\partial T}\frac{\partial T}{\partial P_v}\right) + \lambda_v\right]$$

$$\times\left(\lambda_l h_l - \frac{\lambda}{\dfrac{\partial P_c}{\partial S}}\frac{\partial T}{\partial S} + \lambda_l h_l \frac{\dfrac{\partial P_c}{\partial T}\dfrac{\partial T}{\partial S}}{\dfrac{\partial P_c}{\partial S}}\right) \tag{28}$$

$$-\lambda_l\left(1 + \frac{\dfrac{\partial P_c}{\partial T}\dfrac{\partial T}{\partial S}}{\dfrac{\partial P_c}{\partial S}}\right)\left(\lambda_l h_l + \lambda_v h_v - \lambda_l h_l \frac{\partial P_c}{\partial T}\frac{\partial T}{\partial P_v} + \lambda \frac{\partial T}{\partial P_v}\right) \tag{29}$$

$$\mathscr{G}^* = g \sin\theta\left[\left(\lambda_l\left(1 - \frac{\partial P_c}{\partial P_v}\right) + \lambda_v\right)(Q/(g \sin\theta) + \lambda_l \rho_l h_l + \lambda_v \rho_v h_v)\right. \tag{30}$$

$$\left. -(\lambda_l \rho_l + \lambda_v \rho_v)\left(\lambda_l h_l\left(1 - \frac{\partial P_c}{\partial P_v}\right) + h_v \lambda_v + \lambda \frac{\partial T}{\partial P_v}\right)\right] \tag{31}$$

$$\mathscr{H}^* = -g \sin\theta\left[(Q/(g \sin\theta) + \lambda_l \rho_l h_l + \lambda_v \rho_v h_v)\lambda_l\left(1 + \frac{\dfrac{\partial P_c}{\partial T}\dfrac{\partial T}{\partial S}}{\dfrac{\partial P_c}{\partial S}}\right)\right. \tag{32}$$

$$\left. -(\lambda_l \rho_l + \lambda_v \rho_v)\left(\lambda_l h_l\left(1 + \frac{\dfrac{\partial P_c}{\partial T}\dfrac{\partial T}{\partial S}}{\dfrac{\partial P_c}{\partial S}}\right) - \frac{\lambda}{\dfrac{\partial P_c}{\partial S}}\frac{\partial T}{\partial S}\right)\right] \tag{33}$$

$$P_v^* = P_v/P_0 \tag{34}$$

$$z^* = z/H_0 \tag{35}$$

$$\varepsilon = \frac{1}{P_0}\frac{\partial P_c}{\partial S}. \tag{36}$$

The vertical coordinate z has been non-dimensionalized by dividing by H_0, which might be chosen to be, say, $H_0 = 1000$ m. The non-dimensionalization in ref. [6] is avoided here, as it depends on the temperature or vapor-pressure.

This form of the equations, with a small parameter ε, is useful if the right-hand sides are about the same size in magnitude. Most terms in $\mathscr{H}^*$ are clearly of

the same order of magnitude in size as those in $\mathscr{G}^*$. The exceptions are considered here:

Over the temperature range 100–300°C, numerical calculations reveal that the term $\partial P_c/\partial T\ \partial T/\partial P_v$ has a magnitude less than or equal to $10^{-9}/\sqrt{k}$. This upper bound is much less than one when $k \gg 10^{-18}$ m^2, so for these k values the term $1 - \partial P_c/\partial T\ \partial T/\partial P_v$ will be close to one.

The term

$$\frac{\dfrac{\partial P_c}{\partial T}\dfrac{\partial T}{\partial S}}{\dfrac{\partial P_c}{\partial S}}$$

is less that 0.1 for the temperatures, saturations and permeabilities from 1 d to 0.01 μd considered here, according to numerical calculations, and so may be neglected since it only appears added to the number 1.

The term

$$\lambda\frac{\partial T}{\partial P_v}$$

appears in $\mathscr{G}^*$ in a location that corresponds to that of the term

$$\frac{\dfrac{\lambda}{\dfrac{\partial P_c}{\partial S}}\dfrac{\partial T}{\partial S}}{}$$

in $\mathscr{H}^*$.

Numerical calculations show that these two terms are different in size, with a ratio in the range 10–10^3, increasing as temperature decreases, and practically independent of k. The larger term is the one in $\mathscr{G}^*$. Since both terms are associated with the conductive mechanism, neither is important for large enough k when convection dominates through the other terms. Convection and conduction effects become comparable when

$$\lambda\frac{\partial T}{\partial P_v} = \lambda_l h_l. \tag{37}$$

This occurs first (as k is reduced from 1 d say) when T is 100°C (since the slope of the Clausius–Clapeyron curve is steepest there) and k is approximately 10^{-15} m^2.

Hence for $k \gg 10^{-18}$ m^2, individual convection terms in $\mathscr{G}^*$ are of sizes comparable to the convection terms in $\mathscr{H}^*$, and for $k > 1$ md convection will dominate heat flow. When the pressure range P_0 under consideration is of the order of 10^7 Pa, the size of ε may be estimated by using the Leverett J-function form for P_c [20, 21]

$$P_c = \frac{\sigma(T)}{\sqrt{k}}J(S) \tag{38}$$

to be

$$\varepsilon \sim 10^{-9}/\sqrt{k}. \tag{39}$$

This is less than 3×10^{-2} for $k > 1$ md. ε goes to zero as k increases and as capillarity decreases. Hence the following perturbation analysis is expected to apply when $k > 10^{-15}$ m^2 so that heat flow is convection-dominated. This covers many practical situations in porous medium flow.

The name convection-dominated is a little misleading here, because when small values for heat flow are considered in a later section, another limit in which conduction is important is reached. Then terms with mobility squared are small, and heat flow is comparable to conductive values. Hence in the following analysis conductive terms are retained, and the conclusions reached are valid also for small heat flow rates near conductive values.

4. CONVECTIVE HEAT FLOW

Equations (26) and (27) are suitable for analysis with singular perturbation methods, e.g. [22], when $k > 1$ md. The superscript asterisks will be dropped in what follows. Only leading behaviour is studied here, that is, only the first term in each of the expansions

$$P_v = \sum_{n=0} \varepsilon^n P_{vn} \quad S = \sum_{n=0} \varepsilon^n S_n$$

is calculated.

Solutions to equations (26) and (27) have capillary boundary layers (inner solutions) in narrow regions of thickness ε, and outer solutions (where gravity is more important) elsewhere. These are not the same as the boundary layers studied in [6], which are boundary layers in the Kelvin effect and in conduction, and lie within the capillary boundary layers obtained here. Satik *et al.* ([6], equations 65 and 66) do consider a simplified version of equations (26) and (27), with no Kelvin effect and limited heat flow. However, their outer solutions (the $G = 0$ contours) are very different from those presented here, due presumably to the limited heat flows that a three-layer model allows when the liquid phase is at the bottom, and to the assumption in [6] that fluid properties are independent of temperature.

4.1. *Outer solution*

The outer solution is valid everywhere except in narrow boundary-layer regions, and is obtained by expanding everything in equations (26) and (27) in power series in ε and equating coefficients of powers of ε. The leading behaviour (which may be obtained by setting ε to zero) is:

$$\frac{\partial P_{v0}}{\partial z} = -\left.\frac{\mathscr{H}}{\mathscr{F}}\right|_{\varepsilon=0} \tag{40}$$

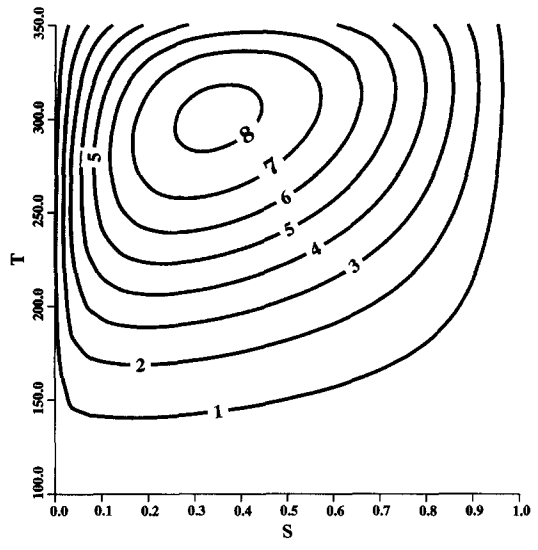

Fig. 2. Outer (gravity-driven) solutions for steady heat pipes. The contours are of constant Q/k in kW dm^{-2}.

$$0 = \left.\frac{\mathscr{G}}{\mathscr{F}}\right|_{\varepsilon=0}. \tag{41}$$

Evaluation at $\varepsilon = 0$ is interpreted to mean at zero capillary pressure. These are exactly the equations for a gravity-driven heat pipe which are derived directly from conservation of mass and energy if capillarity is ignored [10, 13, 23]. Equation (41) requires $\mathscr{G}|_{\varepsilon=0} = 0$. This may be written

$$k_{rl}k_{rv} = k_{rl}\left(\frac{\omega}{\sin\theta} - \frac{\rho_l\lambda}{k}\gamma\right) + k_{rv}\beta\left(\frac{\omega}{\sin\theta} - \frac{\rho_v\lambda}{k}\gamma\right). \tag{42}$$

The term $\sin\theta$ has been assumed to be non-zero. The case that it is zero is the already well-understood engineering heat pipe case.

This equation has appeared in various forms in previous heat pipe studies ([6, 8, 4, 10, 12, 13], where it is called the dryout condition or the solvability condition) and constitutes an *algebraic* relationship between the imposed heat flux, pressure (or temperature) and liquid saturation. Given Q (or the better combination Q/k), it may be solved to relate S and P_{v0}, allowing solution of the differential equation for pressure, equation (40). It is plotted in Fig. 2. Note that for $k > 1$ md, contours of constant Q/k are independent of the value chosen for k. Other parameter values used in Fig. 2 are listed in Table 2. Accurate numerical routines from the code for TOUGH2 [24–26] have been used for calculations, with full temperature and saturation dependence of fluid properties. Note that ω and γ depend on temperature.

Outer (gravity-driven) solutions must track the contours of equation (42) (if they exist) in the temperature-saturation phase plane. When heat flow is too large, outer solutions do not exist.

Table 2. Default parameter values used for numerical calculations in this paper

Parameter	Value	Units
λ	2.0	W m^{-1} °C
ϕ	0.1	
k_{rl}	S	
k_{rv}	1−S	

Note that typically, in the geothermal case, there are two gravity-driven steady solutions, one liquid-dominated and one vapor-dominated. For large enough heat flows, or if heat flow is downwards, there are no gravity-driven solutions. For small heat flows, between the two zeros of the two terms on the right-hand side of equation (42), there is only one (vapor-dominated) gravity-driven solution. This latter case corresponds to that studied in [7], when heat is provided by conduction through a stationary liquid layer below the two-phase zone.

4.2. *Inner solution*

The inner solution applies in the boundary-layer regions, in which saturation is rapidly varying. Making the substitution $Z = z/\varepsilon$, and calling the leading order inner solutions $\mathscr{P}$ and $\mathscr{S}$, the leading order equations are

$$\frac{\partial\mathscr{P}}{\partial Z} = 0 \tag{43}$$

$$\frac{\partial\mathscr{S}}{\partial Z} = \left.\frac{\mathscr{G}}{\mathscr{F}}\right|_{z=0}. \tag{44}$$

(45)

That is, to leading order in ε the vapor pressure is constant in the boundary layers, and the saturation changes according to equation (44). With constant vapor pressure, this is a first-order autonomous ordinary differential equation in $\mathscr{S}$, so that $\mathscr{S}$ moves with Z until a zero of $\mathscr{G}$ is encountered, or until single phase conditions are encountered. Hence the inner solutions match naturally with the outer ($\mathscr{G} = 0$) solutions.

5. SOLUTION SELECTION

The above perturbation analysis indicates that steady heat pipe solutions have two essential characteristics, inner capillary boundary-layers with almost constant vapor pressure, and outer gravity-driven solutions that track the contours of the expression $\mathscr{G} = 0$. Full solutions may consist of one or both of these inner and outer approximations, depending on boundary conditions.

Numerical solution of the full steady-state equations, using the full thermodynamic dependence of

fluid properties, has been carried out using the package called STRIDE ([27]), an implementation of singly-implicit Runge–Kutta methods designed for both stiff and non-stiff systems of ordinary differential equations. These numerical solutions confirm the above comments about solution behaviour. They are plotted in Fig. 3.

Solution trajectories from a variety of initial conditions and integration directions have been combined to generate these plots. Solutions are shown both in the temperature-saturation phase plane and as temperature and saturation vs depth. The zero depth value is arbitrary, and is different for each trajectory. Solution trajectories have been started from a variety of initial conditions (temperature and saturation), at the zero depth, and integrated both forwards and backwards in the spatial direction. Initial conditions typically fall in boundary-layer regions, so the capillary boundary layers are seen as vertical lines near zero depth (and near the ends of trajectories) in the plots of saturation against depth. Positive depth values result for solutions following the vapor-dominated branch of the outer solution, and negative depth values for the liquid-dominated branch.

In Fig. 3 (a) some trajectories cross directly from left to right. These are capillary-driven, and correspond to very short heat pipes. Others meet with a $\mathcal{G} = 0$ contour, and can be much longer. These are predominantly gravity-driven. Note in Figs. 3 (b) and (c), how narrow the capillary boundary-layer regions are (1–2 m) compared with the gravity-driven regions (usually kilometers deep). The gravity-driven regions track closely the $\mathcal{G} = 0$ contours, the differences being indistinguishable in Figs. 3 (a) and (e).

In the geothermal situation, it is usual for temperature and vapor-pressure to increase with depth below ground surface. This is reflected by the fact that for positive $\omega/\sin\theta$, $\mathcal{H}$ and $\mathcal{F}$ are of one sign, so that $\partial P_v/\partial z$ is one-signed. Hence to proceed deeper and deeper below ground is to proceed in the direction of increasing temperature and pressure. The other case, that a porous medium is heated from above, is also possible, but there are no $\mathcal{G} = 0$ (outer) solutions for this case, which is the capillary-driven heat pipe.

Boundary conditions already imposed are zero net mass flux, and constant heat flux. The heat flux satisfies $\omega/\sin\theta > 0$ if there are to exist solutions to $\mathcal{G} = 0$. Then a natural choice of initial conditions for the steady-state equations is to specify constant vapor-pressure and saturation at some initial value of z ($z = 0$ without loss of generality). This choice selects a unique solution trajectory in the pressure-saturation plane. Which solution branch of the $\mathcal{G} = 0$ curve will be seen, clearly depends on whether this initial value is imposed at the top or at the bottom of the heat pipe.

Unless the initial values of pressure and saturation lie very close to or on the left side of the vapor-dominated branch of the $\mathcal{G} = 0$ contour, proceeding from the initial point in the direction of increasing vapor-pressure and temperature clearly corresponds to a solution that in general quickly approaches the liquid-dominated branch. The liquid-dominated solution is *selected* by fixing vapor-pressure and saturation at the top end of a geothermal reservoir (or of a numerical model or a laboratory experiment). The vapor-dominated branch may be regarded as unstable, not in time but in space, when integrating in the direction of increasing vapor-pressure, since it can only be obtained by a careful choice of the boundary values of vapor-pressure and saturation, close to that branch.

Similarly, proceeding in the direction of decreasing vapor-pressure and temperature yields in general solutions that approach the vapor-dominated branch of $\mathcal{G} = 0$, unless initial conditions lie on or to the right of the liquid-dominated branch. The liquid-dominated branch may be regarded as unstable in space, when integrating in the direction of decreasing vapor-pressure.

Note that for small heat flow rates, solutions that follow the $\mathcal{G} = 0$ contours correspond to almost constant saturation solutions.

Initial conditions that lie on the wrong side of $\mathcal{G} = 0$ will approach single phase conditions. An initial condition that lies on the correct side of and very close to the unstable branch of $\mathcal{G} = 0$ will track it for some distance, before departing via an internal boundary layer to the stable branch. Hence it is possible to have a section of liquid-dominated heat pipe underlying a section of vapor-dominated heat pipe, in the geothermal context with hotter fluid lying deeper. This would also be obtained if an internal boundary was used with values of pressure and saturation specified between the two branches of $\mathcal{G} = 0$, and z extended in both directions from the internal boundary condition. It is not possible to have a steady vapor-dominated heat pipe underlying a liquid-dominated one.

6. PREVIOUS STUDIES

In the following subsections the implications of the above perturbation analysis for previous experimental, numerical and analytical studies are explored.

6.1. *Experimental results*

In [4] is reported an experiment with boiling in a vertical cylinder heated from below. The apparatus has an overlying layer of cooled water, so that solutions have a boundary condition at the top with pressure kept near atmospheric and saturation held at 1. Steady solutions illustrated in Fig. 3 then typically track the liquid-dominated branch, consistent with the findings of [5] illustrated in [4], with only liquid-dominated steady solutions observed in practice. Similarly, a water layer is maintained at the top of the apparatus used in [15], and the match between theory and experiment they obtain for non-dimensional steam height vs Nusselt number, relies on an earlier choice of the liquid-dominated solution for S.

It is claimed in [4] that the maximum (dry-out) heat flux is independent of the height of the porous bed. While there is no explicit dependence on height in the formula, there is dependence on pressure or temperature through the thermodynamic quantities h_v, ρ and v. Then since temperature or pressure vary with depth, there is a dependence on bed height, but it will not be seen until lengths of the order of km are attained.

If the heat flux across the porous medium exceeds the dry-out value at that temperature, then the solution trajectory will not meet the $\mathcal{G} = 0$ contour, and will proceed between pure liquid and pure vapor along an inner capillary boundary-layer solution. This is still a two-phase region of vapor–liquid counterflow, but it will be relatively short. The dominant mechanism driving the counter-flow is capillary pressure.

6.2. *Multi-layer models*

When it is required that there be a single-phase liquid region below the two-phase region, the zero net mass flux condition together with the one-dimensional

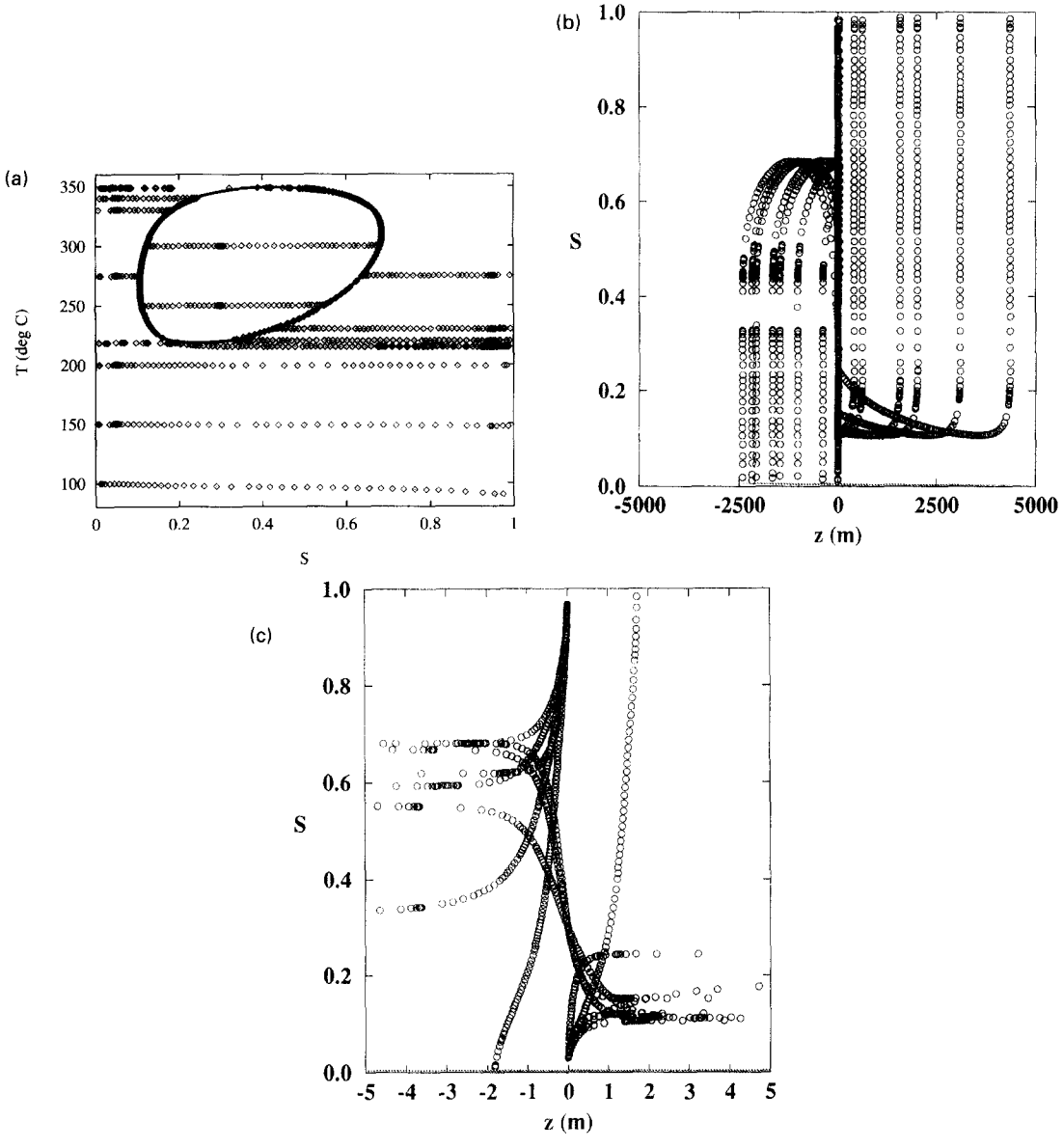

Fig. 3. Accurate numerical solutions for steady heat pipes, obtained by using STRIDE (see text). The solid curves are the outer solutions, and symbols show accurate numerical solution trajectories. Permeability is 1d in all plots. Plot (a) is a temperature-saturation plot of numerical solutions and outer solutions, for $Q/k = 6$ kW dm^{-2}. Plot (b) shows the numerical saturation values from plot (a) against depth. Plot (c) is an expanded depth-scale version of plot (b), showing saturation values in the capillary boundary layers. Plot (d) shows numerical vapor-pressures against depth for solutions in plot (a). Plot (e) shows a temperature-saturation plot for $Q/k = 1$ kW dm^{-2}, for comparison.

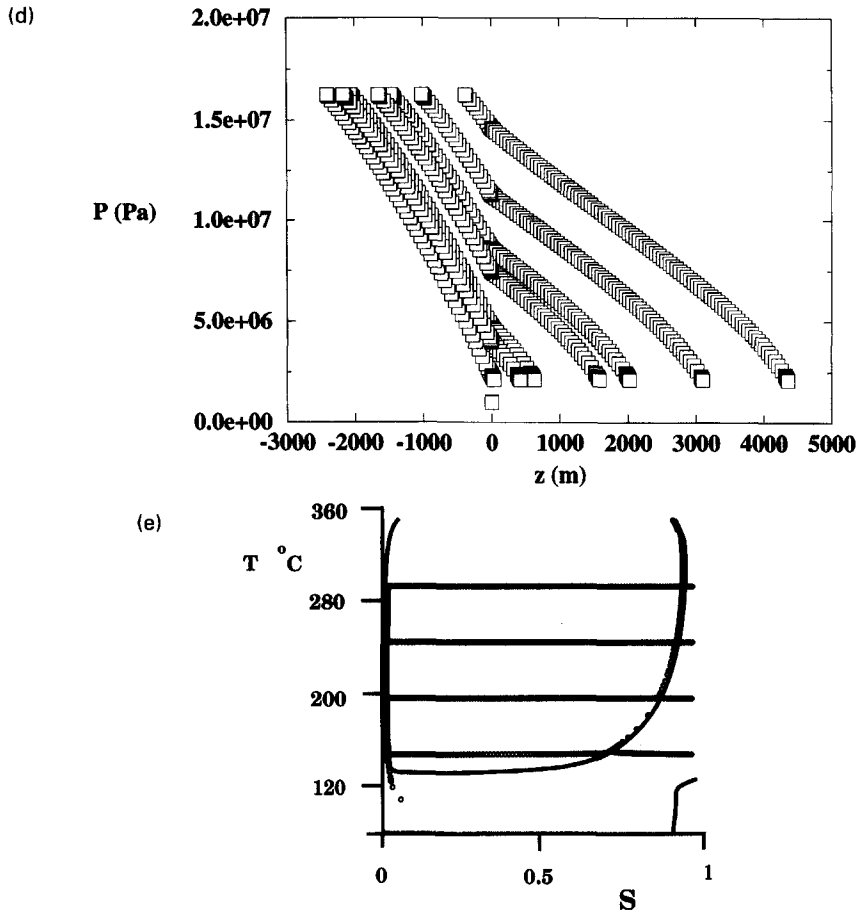

Fig. 3—*continued.*

nature of the model means that heat flow in this two-layer model is restricted to values up to what may be conducted across a quiescent liquid layer, as explained in [7]. This corresponds to the coefficient of k_{rl} [in equation (42) for $\mathcal{G} = 0$] being less than or equal to zero, or $\omega \leqslant \sin\theta\rho_l\lambda\gamma/k$. In this case there is only one or no outer solution branch. A typical example of the phase plane trajectories is illustrated in Fig. 4. There is only one outer solution branch, with small saturation values (vapor-dominated). Saturation varies rapidly in narrow boundary layers in the first metre of depth, then changes only slowly as it tracks the outer solution. Although not shown in this figure, trajectories can also approach the outer solution from the left in the phase plane, that is, from saturation values below 1.0×10^{-5}, in the direction of decreasing temperature.

Note that solutions can only approach the vapor-dominated outer solution in a direction of decreasing temperature. Hence for any model with a quiescent liquid layer below, it is necessary in general to specify the boundary values of pressure and saturation at the hotter (lower) end, if it is hoped to obtain a steady solution that is gravity-driven over any appreciable distance. If boundary conditions are specified at the cooler (upper) end, then very special boundary values of pressure and saturation (that lie on the appropriate contour of $\mathcal{G} = 0$) must be chosen if the solution is to track the gravity-driven outer solution for any appreciable distance.

The two-layer modelling in [7] has boundary conditions imposed at the hotter lower end, with a two-phase region overlying a quiescent liquid region. Saturation is carefully chosen to lie on the single (vapor-dominated) $\mathcal{G} = 0$ contour, and solutions track this branch closely.

A three-layer model with liquid at top and bottom is used in [9]. They find no two-phase region for zero net mass flux. This is consistent with above results, which imply that a solution with an appreciable two-phase region is difficult to obtain when boundary conditions are imposed at the cooler end, as in [9]. This solution would have a jump in saturation at the cooler end, at the interface with the pure liquid phase. Such a jump would not be supported with capillarity present. There is in fact no solution that smoothly connects from $S \approx 1$ to $S = 1$ in the phase plane. Capillary

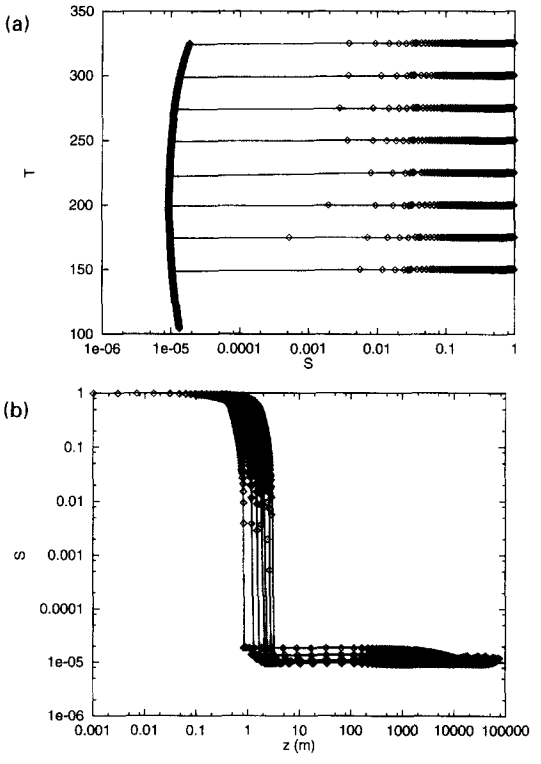

Fig. 4. Typical solution trajectories (a) in the saturation-temperature phase plane and (b) as saturation vs depth, for small heat flow $Q/k = 1$ W dm^{-2}.

effects are not included in [9], but it is possible that the upstream differencing they use for convective terms has the same effect as capillarity, introducing narrow boundary layers ([10, 12, 13]).

In [6] the model is a three-layer one, with liquid at one end and vapor at the other. Capillarity and conductive effects are studied. Numerical integrations are carried out starting from the vapor end. When the liquid end is at the bottom, heat flow rates are restricted to values such that only one solution branch of $\mathscr{G} = 0$ exists, vapor-dominated as discussed above. When the vapor end is at the bottom, this restriction is lifted, but since integration starts at $S = 0$, only vapor-dominated solutions are seen, consistent with comments above.

A curious singularity in the dry-out heat flux is introduced and studied in [6]. It is there concluded that for small enough heat flows, or small enough permeabilities, trajectories in the temperature-saturation phase plane are ill-behaved, and the existence of steady solutions is argued against. This seems to be due to the fact that these trajectories do not cross all the way from vapor to liquid conditions, and reflects the limitation imposed by requiring a three-layer model. For larger permeabilities the singularity presented in [6] is simply due to the appropriate $\mathscr{G} = 0$ contour in the temperature-saturation phase plane growing from a small closed shape until it extends all the way from (say) 100°C to the critical temperature, as heat flow is reduced. Then trajectories cannot cross all the way from $S = 0$ to $S = 1$, and no three-layer solution exists. As permeability is reduced the $\mathscr{G} = 0$ contours behave in a similar manner, as discussed in a later paper ([16]).

7. GENERALITY OF RESULTS

These results are qualitatively independent of the particular form chosen for the relative permeability functions. In particular, the $\mathscr{G} = 0$ contours have the same general shape, for a variety of choices of relative permeabilities, as illustrated in Fig. 5. For smooth enough monotonic relative permeability functions, this may be understood by considering more closely the possible solutions to equation (42). The left and right sides of this equation are sketched in Fig. 6. The term $k_{rl}k_{rv}$ must rise from and return to zero, with a single maximum as illustrated if the relative permeability functions are smooth enough. The right side of equation (42) is a linear combination of the relative permeabilities, the coefficients

$$a = \left(\frac{\omega}{\sin\theta} - \frac{\rho_l \lambda}{k}\gamma\right)$$

and

$$b = \beta\left(\frac{\omega}{\sin\theta} - \frac{\rho_v \lambda}{k}\gamma\right)$$

depending on vapor-pressure and heat flow. Hence the qualitative way in which the left and right sides intersect is not dependent on the particular form chosen for the relative permeability functions, provided they are smooth enough and vary monotonically in the usual way between 0 and 1. To further illustrate this, Fig. 5 shows $\mathscr{G} = 0$ contours calculated explicitly for various choices of these functions. The functions used are detailed in Appendix A. The contours of constant Q/k (kW dm^{-2}) do not vary with k for permeabilities greater than 1 md. A value of $k = 1$ d has been used in these plots, and residual saturations S_r and S_{vr} have been set to zero. In the Sandia curves, δ has been set to 0.5.

8. VISUALIZATION STUDIES

The complicated nature of the right-hand sides of equations (26) and (27) has prompted the use of visualization methods to explore and verify their nature. Of particular interest is the slope of solutions in the saturation-pressure phase plane. The equations are rearranged into the form (leaving out the asterisks)

$$\frac{\partial S}{\partial P_v} = -\frac{\mathscr{G}}{\varepsilon \mathscr{H}}. \tag{46}$$

The $\mathscr{G} = 0$ contours then indicate where the solution slopes, given by the right-hand side of equation (46), are zero. Note that $\mathscr{H}$ cannot take zero values for bottom heating ($Q/\sin\theta > 0$). The size of the solution

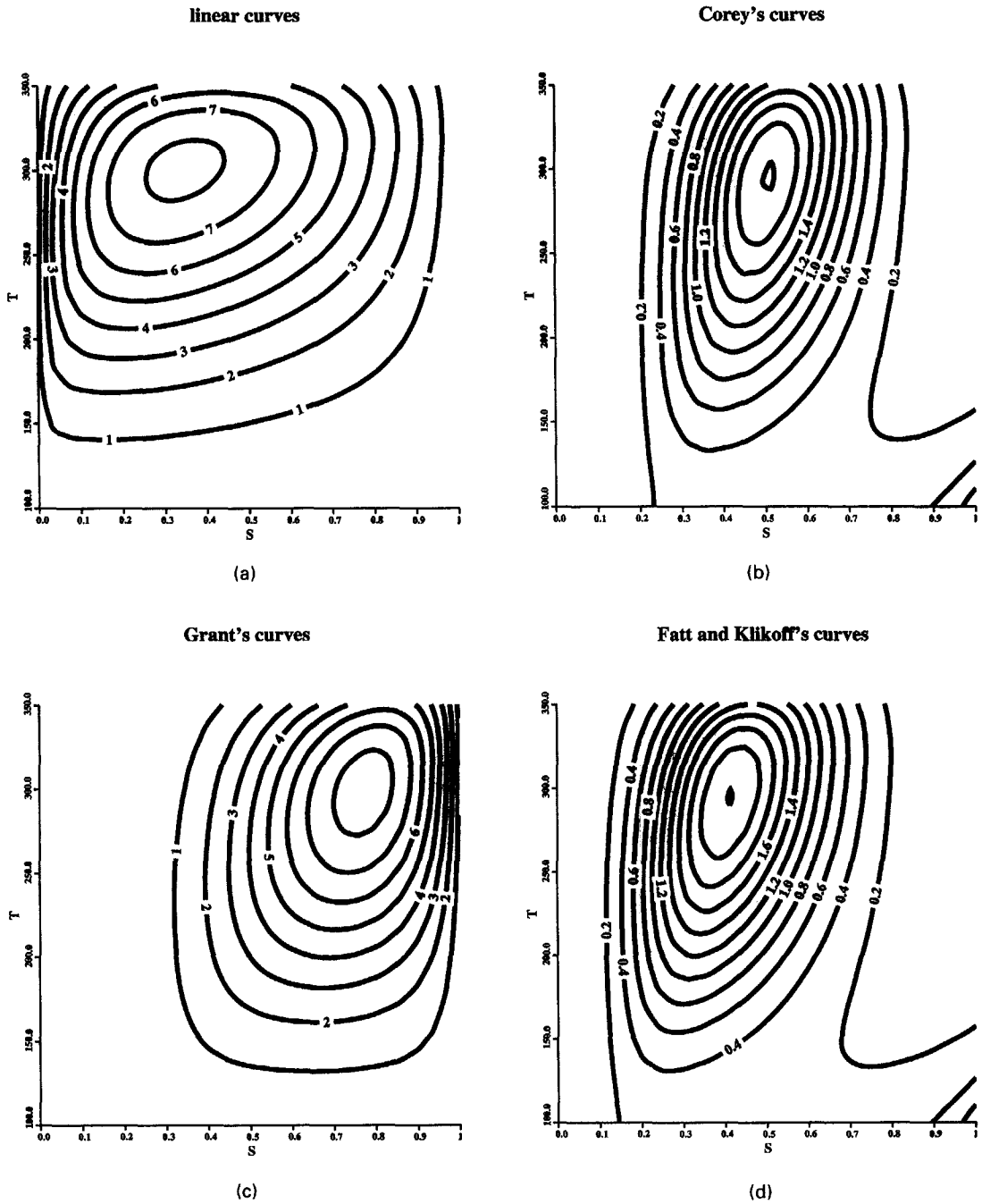

Fig. 5. Outer solutions for a variety of relative permeability functions. The functions used are listed in the Appendix.

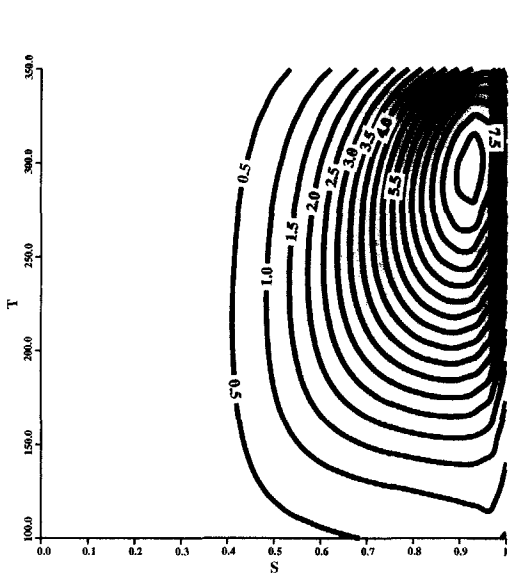

(e)
Fig. 5—*continued.*

slopes is inversely proportional to the size of ε, indicating the usefulness of the perturbation approach taken above. Visualizations have involved calculating the right-hand sides of equation (46) for a range of values of vapor-pressure, saturation and heat flow, and viewing these slopes as scalar data values in a three-dimensional space with coordinates of vapor-pressure, saturation and heat flow over permeability. A Silicon Graphics Iris Indigo workstation was used to do the calculations and the visualizations, using the Iris Explorer software. An isosurface is put through zero values of slope, and level values of this represent the $\mathcal{G} = 0$ contours. Two-dimensional slices with coloured contours representing slope value were moved freely about the 3D region while viewing them on screen, to ensure no unexpected values were present. In this way, it was possible to quickly verify the perturbation approach used above, for large enough permeabilities. In particular, the $\mathcal{G} = 0$ isosurface remains invariant when permeability is varied, and the slope values taken are consistent with the predicted form of ε in equation (39). These visualizations were also useful for investigating what happens as permeability is reduced below the value 10^{-15} m^2 and conduction becomes more important, the subject of a later paper ([16]). Figure 7 illustrates in black and white the kind of information available in these visualizations.

9. LENGTH OF HEAT PIPES

The lengths of geothermal heat pipes may be estimated in the bottom heating case, by using the outer solution and ignoring the relatively narrow boundary layer. This is the case in which it has been speculated that the maximum length of the heat pipe may be infinite ([6, 15, 8]). As may be seen from Fig. 2, when heat flow is small enough that $Q/k < 0.8$ kW dm^{-2}, the outer solutions can extend below 100°C. A consideration of the form of equation (42) for $\mathcal{G} = 0$ contours reveals that these contours must all close as critical temperature is approached from below. This is due to the latent heat of vaporization vanishing at critical temperature, where the distinction between phases vanishes, and ω becomes unbounded. So natural bounds on temperature range are 100–371°C, for geothermal systems. In the calculations performed here, the thermodynamic routines used lose their val-

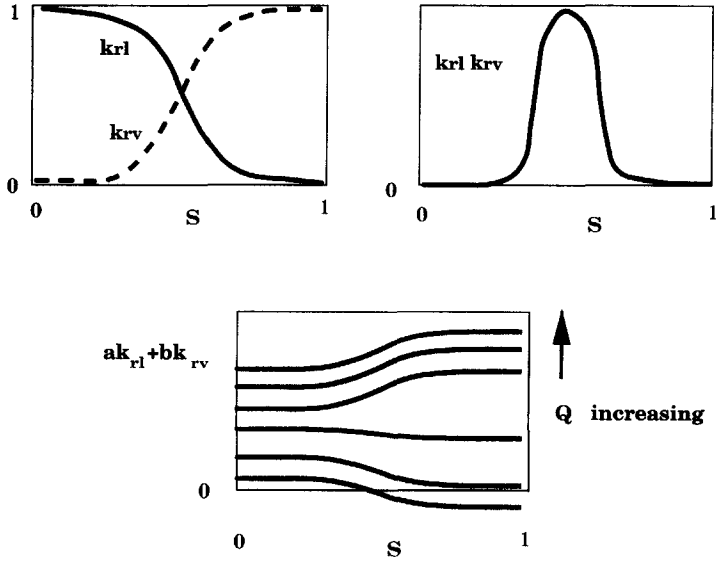

Fig. 6. Sketches of the shapes of the left and right sides of the equation (42) for outer solutions. These shapes are qualitatively correct for all of the major forms of relative permeabilities in the Appendix.

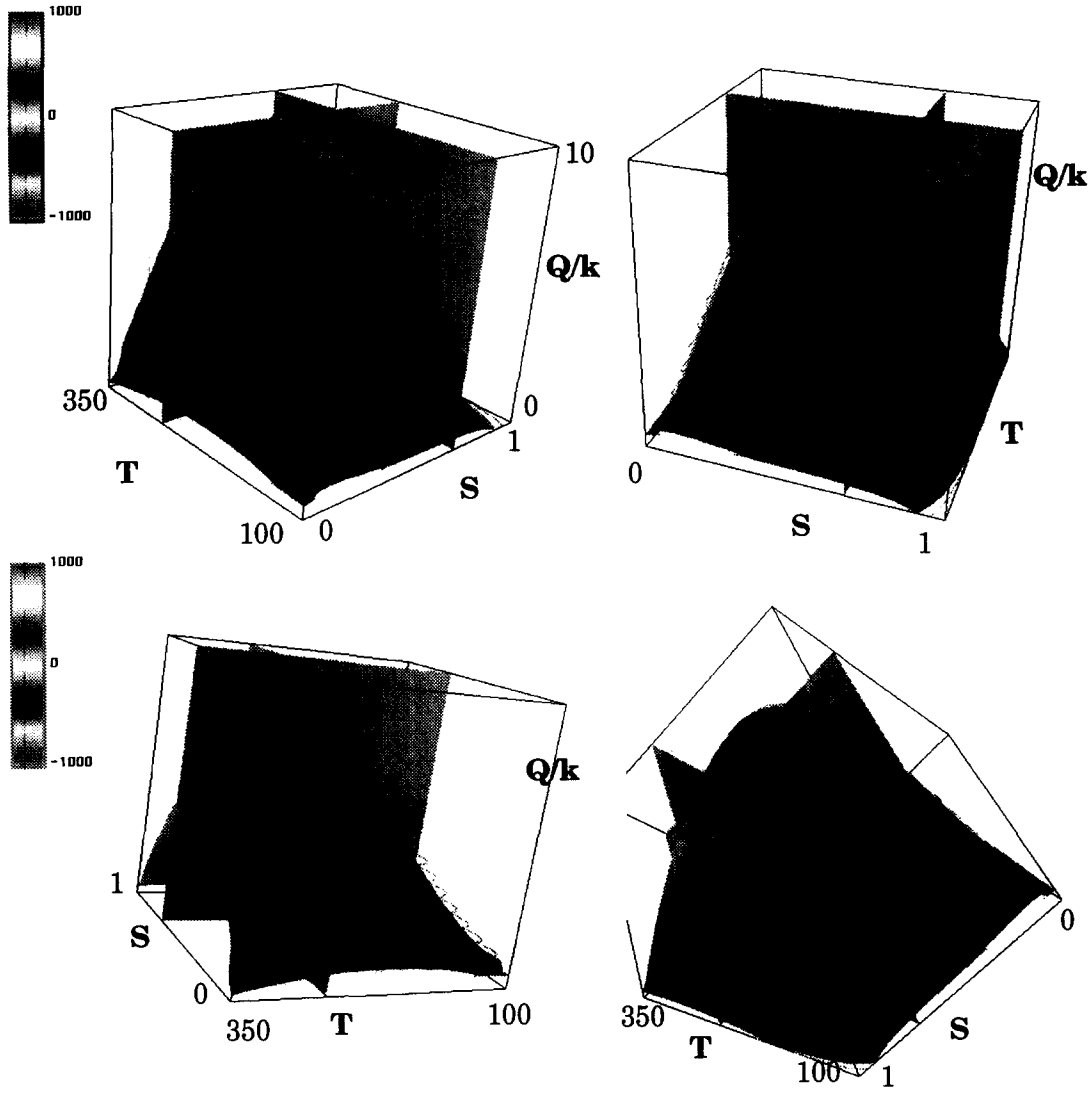

Fig. 7. Visualizations of solution slopes in a three-dimensional space with axes temperature, saturation and heat flow.

idity above 350°C, so this has been used as the upper temperature limit here.

Maximum heat pipe length has been calculated by first expressing equation (40) in the form (dropping the zero subscripts):

$$\frac{\partial P}{\partial z} = -\langle \rho \rangle g \sin\theta \tag{47}$$

where

$$\langle \rho \rangle = \frac{\lambda_v \rho_v + \lambda_l \rho_l}{\lambda_v + \lambda_l} \tag{48}$$

is an effective flowing two-phase density. Capillarity has been set to zero, consistent with the nature of the perturbation approximation, so that $P = P_v = P_l$. Then the maximum heat pipe length is

$$L = \left| \frac{\int dP}{\langle \rho \rangle g \sin\theta} \right| \tag{49}$$

where the integral is taken along one of the two branches of the appropriate $\mathcal{G} = 0$ contour, either over the pressure range corresponding to the temperature range 100–350°C, or from one extreme end of the contour to the other, whichever is the shortest. So there are in general two values for this length, depending on whether the liquid or the vapor-dominated branch is chosen.

The maximum possible length varies with Q/k and with $\sin\theta$, as illustrated in Fig. 8. One effect of reducing $\sin\theta$ below 1 (tilting the column down from vertical) is to reduce the maximum heat flow that may be supported by gravity-driven counterflow. This also leads to the reduction in maximum lengths observed near maximum heat flow, by shrinking the elliptically-shaped contours $\mathcal{G} = 0$. But the dominant effect at lower heat flow values arises from the inverse dependence of L on $\sin\theta$ in equation (49), seen in the increase in L as $\sin\theta$ approaches zero. At lower heat

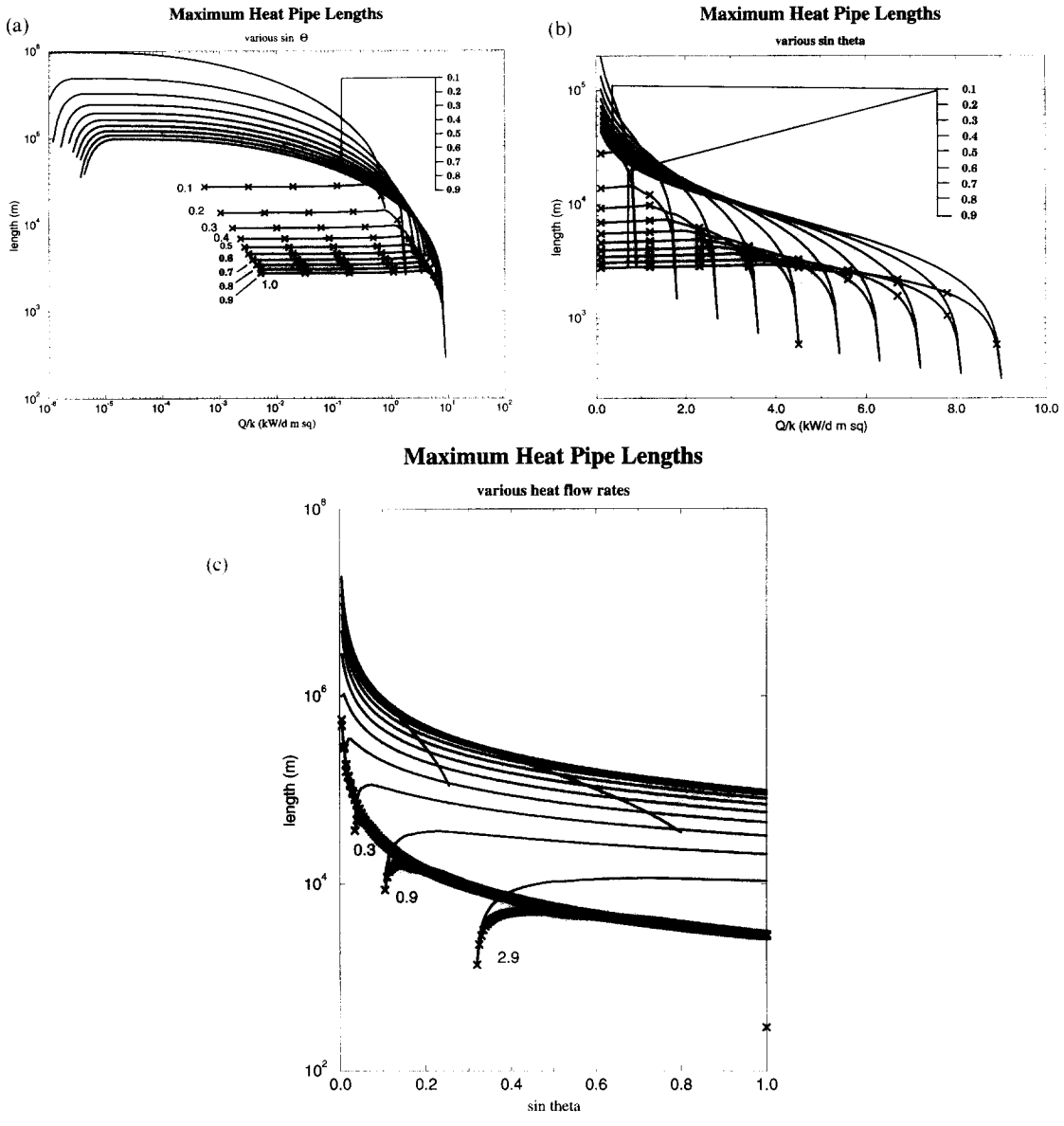

Fig. 8. Maximum possible heat pipe lengths, calculated using only the outer gravity-driven solution curves, and ignoring capillarity. Lengths for vapor-dominated heat pipes have no symbols, while for liquid-dominated heat pipes there are crosses attached. Plot (a) shows length against Q/k for various values of sin θ, plot (b) is the same except the Q/k axis is linear and plot (c) has length against sin θ for various heat flow rates.

flow values, the contours are almost vertical, and close to either immobile liquid or immobile vapor values, so that changes in contour location do not much affect average flowing density.

10. SATURATION—INCREASING OR DECREASING WITH DEPTH

An unusual feature of the interior shocks or boundary layers observed between the $\mathscr{G} = 0$ contours is that saturation increases with increasing temperature or vapor-pressure, rather than decreasing as is characteristic for larger heat flows.

In the usual situation, a liquid saturation that decreases with increasing temperature or pressure is a feature of counterflow that is driven by capillary pressure changes. As liquid saturation decreases, capillary pressure increases, so that liquid pressure decreases, driving liquid in the direction of saturation decrease. This is the direction of increasing temperature. In this case, capillary forces are augmenting gravity drive. The regions in the phase plane that this occurs are shaded in Fig. 9.

In the interior shock, saturation changes are reversed, so that capillary forces oppose gravity forces. The unshaded regions in Fig. 9 where this

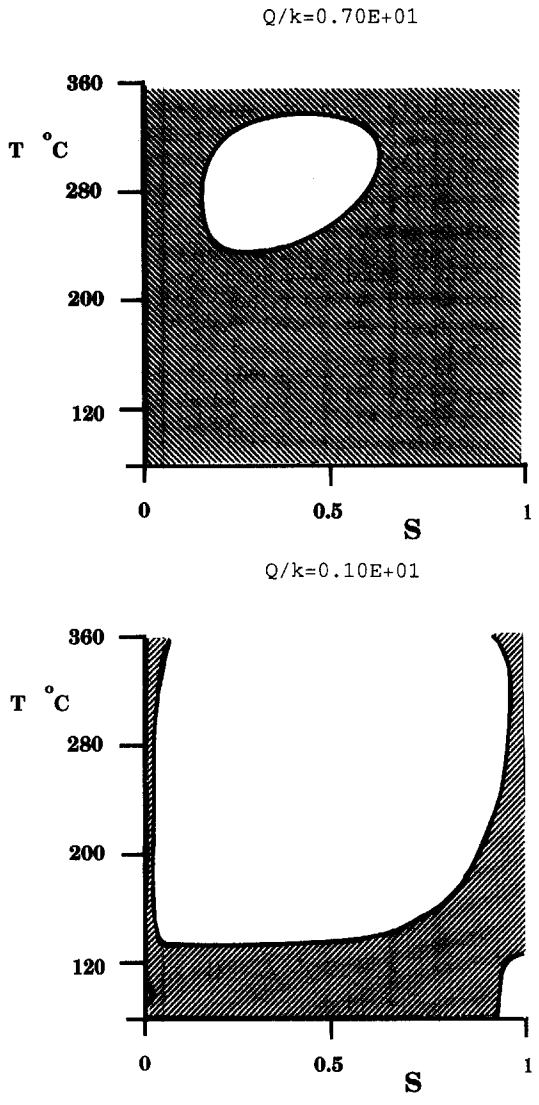

Fig. 9. Regions in the temperature-saturation phase plane are shaded where capillary forces assist gravity forces, for two different values of Q/k (kW dm^{-2}).

occurs are regions where if gravity was the only factor, the steady heat flow would be greater than the imposed boundary value. So capillary acts to counter this. In the shaded regions gravity alone would lead to a steady heat flow that is less than the value imposed at the boundary, so that capillary forces act to boost the heat flow here.

11. SUMMARY

Steady counterflow of steam and liquid through a porous medium has been re-examined, using a single-layer model and singular perturbation techniques, concentrating on the case that convective heat flow is dominant. Typically, solutions move rapidly along capillary boundary layers, and track one of the two possible gravity-driven solutions, vapor-dominated or liquid-dominated. Which solution will be seen depends on boundary conditions. If pressure (or temperature) and saturation are fixed at the top of the porous medium, then typically a liquid-dominated solution is obtained. If pressure (or temperature) and saturation are fixed at the bottom of the porous medium, then typically a vapor-dominated solution is obtained. It is theoretically possible for a liquid-dominated counterflowing region to underlie a vapor-dominated region, with an internal capillary boundary layer between, but it is not possible in terms of this steady one-dimensional model to have the vapor-dominated counterflow underneath the liquid-dominated counterflow.

This has implications for numerical simulations of geothermal reservoirs, for the boundary conditions on actual geothermal reservoirs, and for laboratory experiments. When the reservoir or experiment is open at the top, or in communication with liquid at the top, a liquid-dominated steady heat pipe is to be expected. When the reservoir or experiment is open at the bottom, or in communication with a vapor or liquid region there, a vapor-dominated heat pipe is the expected steady-state.

With these insights, confirmed by detailed numerical solutions and by computer visualizations of solution slopes in the phase plane, it has been possible to understand and explain the varying numerical, experimental and analytical results that have been obtained in the past. It has also been possible to generalize these results to include a variety of forms for relative permeability functions.

Finally, maximum possible lengths for gravity-driven heat pipes have been calculated for different values of heat flow, and the effect of different angles of tilt of the heat pipe has been studied.

This analysis is limited to permeabilities above 1 md, and a further paper is planned to consider the effects of reducing permeability below this value.

Acknowledgements—The visualizations that have led to many of the insights here were performed on equipment provided by support from the Internal Grants Committee of Victoria University of Wellington, and from the New Zealand Lotteries Grants Board. I am grateful to the following people for fruitful discussions: John Harper, Mike O'Sullivan, Karsten Pruess, Jahan Noorishad, Herb Keller, Dan Meiron, Irene Pestov, Steve White, Graham Weir, Roger Young, John Burnell and Warwick Kissling.

REFERENCES

1. D. E. White, J. P. Muffler and A. H. Truesdell, Vapor-dominated hydrothermal systems compared with hot-water systems, *Econ. Geology* **66**, 75–97 (1971).
2. A. Faghri, D. B. Reynolds and P. Faghri, Heat pipes for hands, *Mech. Engng* **111**(6), 70–74 (1989).
3. D. A. Pruzan, L. K. Klingensmith, K. E. Torrance and C. T. Avedisian, Design of high-performance sintered-wick heat pipes, *Int. J. Heat Mass Transfer* **34**(6), 1417–1427 (1991).
4. H. H. Bau and K. E. Torrance, Boiling in low-permeability porous materials, *Int. J. Heat Mass Transfer* **25**, 45–54 (1982).

5. K. Cornwell, B. G. Nair and T. D. Patten, Observation of boiling in porous media, *Int. J. Heat Mass Transfer* **19**, 236–238 (1976).
6. C. Satik, M. Parlar and Y. C. Yortsos, A study of steady-state steam–water counterflow in porous media, *Int. J. Heat Mass Transfer* **34**(7), 1755–1772 (1991).
7. G. Schubert and J. M. Straus, Steam–water counterflow in porous media, *J. Geophys. Res.* **84**, 1621–1628 (1979).
8. K. S. Udell, Heat transfer in porous media considering phase change and capillarity—the heat pipe effect, *Int. J. Heat Mass Transfer* **28**, 485–495 (1985).
9. J. P. Sheu, K. E. Torrance and D. L. Turcotte, On the structure of two-phase hydrothermal flows in porous media, *J. Geophys. Res.* **84**(B13), 7524–7532 (1979).
10. M. J. McGuinness, M. Blakeley, K. Pruess and M. J. O'Sullivan, Geothermal heat pipe stability: solution selection by upstreaming and boundary conditions, *Transport in Porous Media* **11**, 71–100 (1993).
11. M. J. McGuinness, Unstable heat pipes, *Proceedings of the 9th New Zealand Geothermal Workshop*, pp. 147–152. Auckland University (November 1987).
12. M. J. McGuinness, Heat pipe stability and upstream differencing, *Proceedings of the 10th New Zealand Geothermal Workshop*, pp. 117–121, Auckland University (November 1988).
13. M. J. McGuinness, Heat pipe stability in geothermal reservoirs, *Proceedings of the* 1990 *Geothermal Symposium*, Part I, pp. 1301–1308, GRC, Hawaii (1990).
14. A. K. Stubos, C. Satik and Y. C. Yortsos, Effects of capillary heterogeneity on vapor–liquid counterflow in porous media, *Int. J. Heat Mass Transfer* **36**(4), 967–976 (1993).
15. C. H. Sondergeld and D. L. Turcotte, An experimental study of two-phase convection in a porous medium with applications to geological problems, *J. Geophys. Res.* **82**(14), 2045–2053 (1977).
16. M. J. McGuinness, Steady solution selection and existence in geothermal heat pipes—II. The conductive case (in preparation).
17. N. E. Edlefsen and A. B. C. Anderson, Thermodynamics of soil moisture, *Hilgardia* **15**(2), 231–298 (1948).
18. R. McKibbin and K. Pruess, Some effects of non-condensible gas in geothermal reservoirs with steam-water counterflow, *Geothermics* **18**(3), 367–375 (1989).
19. J. C. Martin, R. E. Wegner and F. J. Kelsey, One-dimensional convective and conductive geothermal heat flow, *Proceedings of the 2nd Workshop on Geothermal Reservoir Engineering*, pp. 251–262, Stanford University (1976).
20. M. C. Leverett, Capillary behaviour in porous solids, *AIME Trans.* **142**, 52 (1941).
21. K. S. Udell, Heat transfer in porous media heated from above with evaporation, condensation and capillary effects, *J. Heat Transfer* **105**, 485–492 (1983).
22. C. M. Bender and S. A. Orszag, *Advanced Mathematical Methods for Scientists and Engineers*. McGraw-Hill, New York (1978).
23. M. J. McGuinness, Solution selection in geothermal heat pipes, presented at the 13th New Zealand Geothermal Workshop (1991), and published in *Proceedings of the 14th New Zealand Geothermal Workshop*, pp. 321–326. Auckland University (November 1992).
24. K. Pruess, SHAFT, MULKOM, TOUGH: a set of numerical simulators for multiphase fluid and heat flow, *Geotermia, Rev. Mex. Geoenergia* **4**(1), 185–202 (1988).
25. K. Pruess, TOUGH User's Guide, report LBL-20700, Earth Sciences Division, Lawrence Berkeley Laboratory, University of California, Berkeley, CA 94720, U.S.A.
26. T. Sato, T. Minamiyama and J. Yata, A formulation of the thermodynamic properties of ordinary water substance, *Kyoto Univ. Faculty Engng Mem.* **29**(1), 16–27 (1967).
27. J. C. Butcher, K. Burrage and F. H. Chipman, STRIDE Package for Differential Equations, Mathematics Department, University of Auckland, New Zealand, email chipman @mat.aukuni.ac.nz (1991).

APPENDIX: RELATIVE PERMEABILITY CURVES

This appendix contains expressions for the relative permeability functions used to help check the generality of the approach used in this paper. Outer solutions are plotted in Fig. 5 for each of these functions. These curves have been taken from [25].

Linear functions

$$k_{rl} = S \quad k_{rv} = 1 - S$$

Corey's curves

$$k_{rl} = (S^*)^4 \quad k_{rv} = (1 - S^*)^2(1 - [S^*]^2)$$

where $S^* = (S - S_r)/(1 - S_r - S_{vr})$ and S_r is the residual liquid saturation, S_{vr} is the residual vapor saturation and $S_r + S_{vr} < 1$.

Grant's curves

$$k_{rl} = (S^*)^4 \quad k_{rv} = (1 - k_{rl})$$

where S^* is as defined above.

Fatt and Klikoffs' curves

$$k_{rl} = (S^*)^3 \quad k_{rv} = (1 - S^*)^3$$

where $S^* = (S - S_r)/(1 - S_r)$ and S_r is the residual liquid saturation.

Sandia curves

$$k_{rl} = \begin{cases} \sqrt{S^*}\{1 - (1 - [S^*]^{1/\delta})^{\delta}\}^2 & S < S_s \\ 1 & S \geqslant S_s \end{cases}$$

$$k_{rv} = 1 - k_{rl}$$

where $S^* = (S - S_r)/(S_{vr} - S_r)$, S_r is the residual liquid saturation and S_{vr} is the residual vapor saturation.